

# SCIENTIFIC REPORTS

OPEN

## Theory of Large Intrinsic Spin Hall Effect in Iridate Semimetals

Adarsh S. Patri<sup>1</sup>, Kyusung Hwang<sup>1,2</sup>, Hyun-Woo Lee<sup>1,3</sup> & Yong Baek Kim<sup>1</sup>

We theoretically investigate the mechanism to generate large intrinsic spin Hall effect in iridates or more broadly in 5d transition metal oxides with strong spin-orbit coupling. We demonstrate such a possibility by taking the example of orthorhombic perovskite iridate with nonsymmorphic lattice symmetry, SrIrO<sub>3</sub>, which is a three-dimensional semimetal with nodal line spectrum. It is shown that large intrinsic spin Hall effect arises in this system via the spin-Berry curvature originating from the nearly degenerate electronic spectra surrounding the nodal line. This effect exists even when the nodal line is gently gapped out, due to the persistent nearly degenerate electronic structure. The magnitude of the spin Hall conductivity is shown to be comparable to the best known example such as doped topological insulators and the biggest in any transition metal oxides. To gain further insight, we compute the intrinsic spin Hall conductivity in both bulk and thin film systems. We find that the geometric confinement in thin films leads to significant modifications of the electronic states, leading to even bigger spin Hall conductivity in certain cases. We compare our findings with the recent experimental report on the discovery of large spin Hall effect in SrIrO<sub>3</sub> thin films.

Relativistic spin-orbit coupling (SOC), once relegated to the annals of atomic physics, has become prevalent in modern condensed matter physics. The spin Hall effect<sup>1</sup>, as well as its once-contentious cousin the anomalous Hall effect<sup>2</sup>, are examples of phenomena that are deeply rooted in the physics of SOC. In the spin Hall effect (SHE), an unpolarized electron charge current passing through a material which possesses strong SOC gives rise to a purely spin polarized current in the transverse direction; the inverse spin Hall effect (ISHE) is, as the name suggests, the inverse process where a pure spin current gives rise to a transverse charge current<sup>1,3–6</sup>.

The SHE can be broadly classified under two regimes: intrinsic (which is dependent solely on band topology and SOC) and extrinsic (where impurity scattering is key)<sup>1,7</sup>. A common figure of merit used to examine the efficiency of the spin/charge current conversion is the spin Hall angle:  $\theta_{\text{SH}} = \sigma_{\text{SH}}/\sigma$ , where  $\sigma_{\text{SH}}$  and  $\sigma$  are the respective spin-Hall and charge conductivities<sup>8</sup>. Large SHE has primarily been predicted and/or observed in heavy elemental metals (that possess large SOC) such as Pt<sup>9–15</sup>, Au<sup>9,10,16</sup> (although the origin of the observed large SHE in Au<sup>17</sup> is still under debate<sup>18–20</sup>), and Pd<sup>9,10,21</sup>. More recently, there have also been suggestions of large SHE in topological insulators from spin-torque measurements in topological insulator Bi<sub>2</sub>Se<sub>3</sub><sup>22</sup> and Cr-doped Bi<sub>2</sub>Se<sub>3</sub> thin films<sup>23</sup>. However, despite these two classes of materials demonstrating such large SHEs, they do have their respective drawbacks: the large charge conductivity of the heavy metals hinders their efficiency as spin current detectors (since the spin Hall resistivity, a figure of merit for spin detection, is proportional<sup>24</sup> to  $\sigma_{\text{SH}}/\sigma^2$ ), and the coupling of magnetic layers to topological insulator thin films once again forms a bottleneck for the spin current generation efficiency<sup>22</sup>. In an attempt to achieve a large spin Hall angle with better efficiency, a new class of 5d transition metal oxides has recently been investigated<sup>24</sup>. These materials not only have large SOC (due to the 5d nature of the conduction bands) but are also useful due to their tunability of their physical properties via their magnetic ordering and/or correlation effects<sup>25–27</sup>. Moreover, the emergent semimetallic nature of numerous types of iridates<sup>26–31</sup> provides hope that the spin Hall angle for the iridates will be superior to that of the heavy elemental metals, due to semimetals' relatively smaller charge conductivity.

In this work, we theoretically investigate the intrinsic spin Hall effect in orthorhombic perovskite SrIrO<sub>3</sub>, which is a 5d transition metal oxide with strong SOC. Our work is motivated by recent experimental work on SrIrO<sub>3</sub> thin films, where one of the largest ever recorded spin Hall conductivity was measured<sup>32</sup>. Interestingly, SrIrO<sub>3</sub> possesses a topological nodal line (a loop of band crossings) that is protected by nonsymmorphic symmetries<sup>28,29,33–37</sup>. As shown later, the persistent nearly degenerate electronic structure near the nodal line plays an

<sup>1</sup>Department of Physics and Centre for Quantum Materials, University of Toronto, Toronto, Ontario, M5S 1A7, Canada. <sup>2</sup>Department of Physics, The Ohio State University, Columbus, OH, 43210, USA. <sup>3</sup>PCTP and Department of Physics, Pohang University of Science and Technology, Pohang, 37673, Korea. Correspondence and requests for materials should be addressed to Y.B.K. (email: [ybkim@physics.utoronto.ca](mailto:ybkim@physics.utoronto.ca))

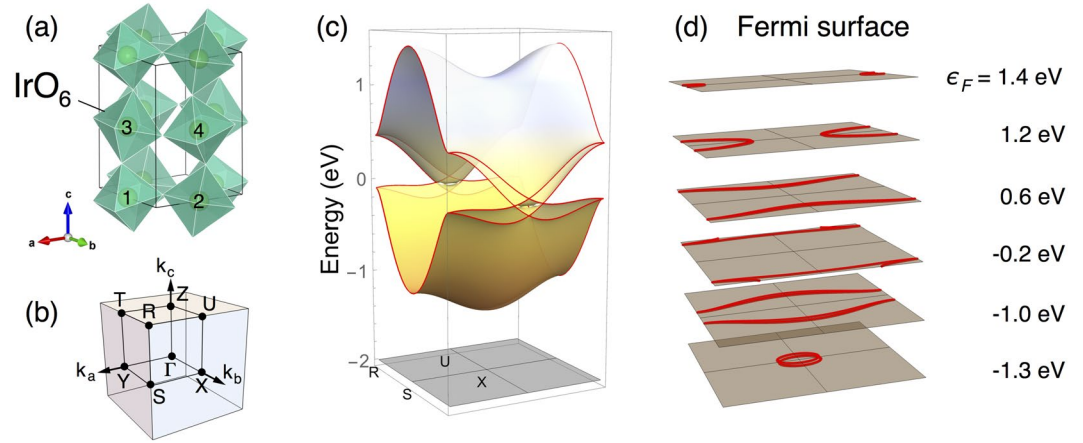


**Figure 1.** Crystal structure and electron energy bands of orthorhombic perovskite SrIrO<sub>3</sub>. **(a)** Orthorhombic unit cell with four Ir sublattices (numbered) and oxygen octahedra surrounding the Ir sites. **(b)** Brillouin zone, with labelled points  $Y = (\pi, 0, 0)$ ,  $X = (0, \pi, 0)$ ,  $Z = (0, 0, \pi)$ ,  $R = (\pi, \pi, \pi)$ ,  $U = (0, \pi, \pi)$  in the coordinate of  $(k_a, k_b, k_c) [= (\mathbf{k} \cdot \mathbf{a}, \mathbf{k} \cdot \mathbf{b}, \mathbf{k} \cdot \mathbf{c})]$  where  $\{\mathbf{a}, \mathbf{b}, \mathbf{c}\}$  are the orthorhombic lattice vectors. **(c)** Electron energy bands at the  $k_b = \pi$  plane (R-U-X-S) of the Brillouin zone. **(d)** Fermi surface cross sections within the  $k_b = \pi$  plane for various Fermi energies.

important role in the SHE in SrIrO<sub>3</sub>. We study the SHE in the framework of linear response theory, focusing on both the bulk system as well as thin film configurations to enable comparison with experiment. In both cases, we compute the spin Hall conductivity by utilizing the  $j_{\text{eff}} = 1/2$  tight binding model constructed from *ab initio* studies of SrIrO<sub>3</sub><sup>28,29</sup>. For the bulk system, we also consider the impact of breaking various nonsymmorphic symmetries of the *Pbnm* space group on the spin Hall conductivity. In this way, we are able to study the robustness of the spin Hall conductivity to a variety of symmetry breaking perturbations. Finally, we consider (010)<sub>c</sub> thin film of SrIrO<sub>3</sub>, where pseudo-cubic coordinate system is used to describe the thin film direction, which enables a more direct connection to the recent experimental work.

### Model Hamiltonian

We employ the tight-binding model constructed in Refs<sup>28,29</sup> to describe the electronic structure of SrIrO<sub>3</sub>. Due to the significant tilting and rotation of oxygen octahedra, the system has the orthorhombic perovskite crystal structure with four Ir sublattices and *Pbnm* nonsymmorphic space group (Fig. 1). In the basis of the  $j_{\text{eff}} = 1/2$  states for Ir<sup>4+</sup> electrons, the model incorporates various electron hopping channels allowed in the orthorhombic perovskite SrIrO<sub>3</sub> with the following form of Hamiltonian.

$$H = \sum_{\mathbf{k}} \psi_{\mathbf{k}}^{\dagger} H_{\mathbf{k}} \psi_{\mathbf{k}}. \quad (1)$$

Here,  $\psi = (\psi_{1\uparrow}, \psi_{2\uparrow}, \psi_{3\uparrow}, \psi_{4\uparrow}, \psi_{1\downarrow}, \psi_{2\downarrow}, \psi_{3\downarrow}, \psi_{4\downarrow})^T$  are electron operators with the subscripts referring to the Ir sublattice (1,2,3,4) and  $j_{\text{eff}} = 1/2$  pseudo-spin ( $\uparrow, \downarrow$ ), and  $\mathbf{k}$  is crystal momentum.

The matrix  $H_{\mathbf{k}}$  contains ten different hopping channels up to the second nearest neighbor. Depending on whether the pseudo-spin changes during hopping processes or not, the hopping channels are classified into spin-dependent hopping  $\{t'_{p}, t_{1p}^o, t_{2p}^o, t_z^o, t_d^o\}$  and spin-independent hopping  $\{t_p, t_x, t_y, t_b, t'_{d'}\}$ . The oxygen octahedron tilting and rotation generate the spin-dependent hopping which is crucial for the SHE in SrIrO<sub>3</sub>. Such spin-dependent hopping is not allowed in the perfect cubic perovskite. For the hopping parameters, we use the values<sup>28</sup> based on *ab initio* calculations. The explicit form of  $H_{\mathbf{k}}$  and values of the hopping parameters are provided in Supplementary A. The *Pbnm* space group symmetry dictates the relations between the components of the spin Hall conductivity tensor, as well as protects various features of the band structure. In Table 1, we summarize the *Pbnm* space group symmetry, as well as the remaining symmetries in various symmetry-broken bulk systems (section: Impact of Breaking Nonsymmorphic Symmetries on Bulk SHC) and thin film (section: Spin Hall Effect in Thin Film System).

Figure 1 depicts the electron band structure of the system at the particular  $k_b = \pi$  plane (R-U-X-S) in the Brillouin zone. There are four doubly degenerate bands on account of four sublattices and Kramers degeneracy. One remarkable feature is the band crossing occurring along a ring about the U point<sup>28,29</sup>. This “nodal ring” is quite small, but protected by nonsymmorphic symmetries compatible with the  $k_b = \pi$  plane<sup>33</sup>. Another interesting point is the “near-degeneracy” of the four bands found at the  $k_b = \pi$  plane and  $k_a = \pi$  plane (T-R-S-Y) as highlighted by cyan in Fig. 2. It must be noted both features appear by spin-dependent electron hopping in the system. Interestingly, the nearly degenerate structure and the size of the nodal ring are correlated and controlled by the same hopping parameter  $t_d^o$ . In fact, this intimate correlation between the two features prevails in a wide window of permissible values of  $t_d^o$ , so that the ring appears concurrently with the presence of the nearly degenerate structure (provided the necessary nodal ring symmetry is intact). Even when the ring is gently gapped out (as will be seen) the nearly degenerate structure is preserved.

Symmetry	$\mathbf{R}'$	$H + h_{gap}$ [Bulk]	$H + h_{xz}$ [Bulk]	$H + h_{xx}$ [Bulk]	$(010)_c$ [Film]
$n$ -glide ( $G_n$ )	$a + \frac{1}{2}, -b + \frac{1}{2}, c + \frac{1}{2}$				
$b$ -glide ( $G_b$ )	$-a + \frac{1}{2}, b + \frac{1}{2}, c$		✓	✓	
Mirror ( $m$ )	$a, b, -c + \frac{1}{2}$	✓			✓
Inversion ( $\bar{1}$ )	$-a, -b, -c$	✓	✓	✓	✓
$a$ -screw ( $S_a$ )	$a + \frac{1}{2}, -b + \frac{1}{2}, -c$		✓	✓	
$b$ -screw ( $S_b$ )	$-a + \frac{1}{2}, b + \frac{1}{2}, -c + \frac{1}{2}$				
$c$ -screw ( $S_c$ )	$-a, -b, c + \frac{1}{2}$	✓			✓

**Table 1.**  $Pbnm$  space group symmetry and remaining symmetries in various symmetry-broken systems. In the second column, the symmetry operations are defined by the transformation rules of the position vector ( $\mathbf{R} = a\hat{a} + b\hat{b} + c\hat{c} \rightarrow \mathbf{R}' = a'\hat{a} + b'\hat{b} + c'\hat{c}$ ). The last four columns represent the remaining symmetries in the symmetry-broken bulk systems (section: Impact of Breaking Nonsymmorphic Symmetries on Bulk SHC) and  $(010)_c$  thin film (section: Spin Hall Effect in Thin Film System) with checkmarks. Representations of the symmetry operations in the basis of electron operators are provided in Supplementary B.

Such a correlated structure, however, will eventually be suppressed by a large perturbation which may significantly modify the underlying band structure. The nodal ring is protected so long as the nonsymmorphic symmetries  $\{G_n, G_b, S_a\}$  are preserved in the system (Supplementary C reviews the symmetry-protection of the nodal line). Although breaking of the  $n$ -glide symmetry gaps out the nodal ring, the presence of additional nonsymmorphic symmetries can tune the nodal ring into Weyl or Dirac point nodes<sup>29,38</sup>. This situation occurs when the  $n$ -glide and mirror symmetries are broken while preserving the  $b$ -glide symmetry. To completely gap out the nodal ring at all points, requires both the  $n$ -glide and  $b$ -glide symmetries to be broken.

### Spin Hall Effect in Bulk System

Intrinsic spin Hall effect in SrIrO<sub>3</sub> is investigated with a linear response theory. We compute the spin Hall conductivity (SHC) tensor  $\sigma_{\mu\nu}^\rho$  using the Kubo formula<sup>1,12</sup>:

$$\sigma_{\mu\nu}^\rho = \frac{2e\hbar}{V} \sum_{\mathbf{k}} \sum_{\varepsilon_{\mathbf{nk}} < \varepsilon_F < \varepsilon_{\mathbf{mk}}} \text{Im} \left[ \frac{\langle \mathbf{mk} | \mathcal{J}_\mu^\rho | \mathbf{nk} \rangle \langle \mathbf{nk} | J_\nu | \mathbf{mk} \rangle}{(\varepsilon_{\mathbf{mk}} - \varepsilon_{\mathbf{nk}})^2} \right]. \quad (2)$$

In this expression,  $J_\nu = \left( = \sum_{\mathbf{k}} \psi_{\mathbf{k}}^\dagger \frac{\partial H_{\mathbf{k}}}{\partial k_\nu} \psi_{\mathbf{k}} \right)$  is the charge current, and  $\mathcal{J}_\mu^\rho = \left( = \frac{1}{4} \{ \sigma^\rho, J_\mu \} \right)$  is the spin current with the  $j_{\text{eff}} = 1/2$  represented by the Pauli matrix  $\sigma^\rho$ . Other quantities in the expression are: the volume  $V$  of the system, Bloch state  $|\mathbf{nk}\rangle$  with energy  $\varepsilon_{\mathbf{nk}}$ , and Fermi level  $\varepsilon_F$ . The spin Hall conductivity connects an applied electric field  $E^\nu$  with an induced transverse spin current by the relationship  $\langle \mathcal{J}_\mu^\rho \rangle = \sigma_{\mu\nu}^\rho E^\nu$ . Here, the three indices imply the direction of the applied electric field or charge current ( $\nu$ ), the direction of the induced spin current ( $\mu$ ), and the spin polarization axis of the spin current ( $\rho$ ). The spin Hall conductivity can be recast as  $\sigma_{\mu\nu}^\rho = \sum_{\mathbf{n}, \mathbf{k}} [\Omega_{\mu\nu}^\rho]_{\mathbf{nk}} f_{\mathbf{nk}}$  with the spin-Berry curvature  $[\Omega_{\mu\nu}^\rho]_{\mathbf{nk}}$  and the electron occupation number  $f_{\mathbf{nk}}$  at energy level  $\varepsilon_{\mathbf{nk}}$ <sup>1,12</sup>. It is the spin-Berry curvature that generates the transverse spin current as an intrinsic effect of electron band structure (analogous to the Berry curvature in anomalous Hall effect). However, in contrast to the anomalous Hall effect, the spin Hall conductivity is even under time reversal, and so the spin Hall effect does not require time reversal to be broken. In our calculations, the configuration  $\{\rho, \mu, \nu\}$  representing the spin Hall effect geometry is specified using the pseudo-cubic axes  $\{\mathbf{x} = (\mathbf{a} - \mathbf{b})/2, \mathbf{y} = (\mathbf{a} + \mathbf{b})/2, \mathbf{z} = \mathbf{c}/2\}$  rather than the orthorhombic lattice vectors  $\{\mathbf{a}, \mathbf{b}, \mathbf{c}\}$ . By employing the pseudo-cubic axes, it enables easier visualization of the symmetry transformations of the spin Hall conductivity tensor. To avoid confusion about the convention, we explicitly write the correspondence between the pseudo-cubic (c) and orthorhombic (o) axes:

$$[100]_c = [1\bar{1}0]_o, [010]_c = [110]_o, [001]_c = [001]_o. \quad (3)$$

We present the spin Hall conductivity  $\sigma_{\mu\nu}^\rho$  in Fig. 2 (right) as a function of the Fermi level  $\varepsilon_F$ . Our results show unexpectedly large spin Hall conductivity of the order of  $10^4(\hbar/e)(\Omega m)^{-1}$  in the three configurations,  $\sigma_{zx}^y, \sigma_{zy}^y, \sigma_{xz}^x$ . To be specific,  $\sigma_{zx}^y$  (red dot) has large values over an extended region except around the zero Fermi energy, while  $\sigma_{zy}^y$  (green triangle) and  $\sigma_{xz}^x$  (orange square) peak around the zero energy. The zero energy is of particular interest as it corresponds to the electron filling of the bulk system (i.e., half filled  $j_{\text{eff}} = 1/2$  electron energy bands). By comparing the spin Hall conductivity with the electron band structure on the left of Fig. 2, one can notice that large values of  $\sigma_{zx}^y$  arise in the energy range that the aforementioned nearly degenerate bands (cyan) are extended over. On the other hand, the peaks of  $\sigma_{zy}^y$  and  $\sigma_{xz}^x$  occur within the energy band width at the UR line (magenta). This implies that the nearly degenerate bands forming the nodal ring structure are closely related to large spin Hall effect in the system. Interestingly,  $Pbnm$  nonsymmorphic symmetries of the bulk system provide useful constraints on the spin Hall conductivity tensor:  $\sigma_{zx}^y = -\sigma_{zy}^x, \sigma_{zy}^y = -\sigma_{zx}^x$ , and  $\sigma_{xz}^x = -\sigma_{yz}^y$ . Hence, the three configurations shown in Fig. 2 are symmetry-related to other three. We present further signatures of nonsymmorphic symmetries in bulk SHC in Supplementary D. Except the aforementioned six configurations, we find subdominant spin Hall conductivity, at least one order of magnitude smaller.

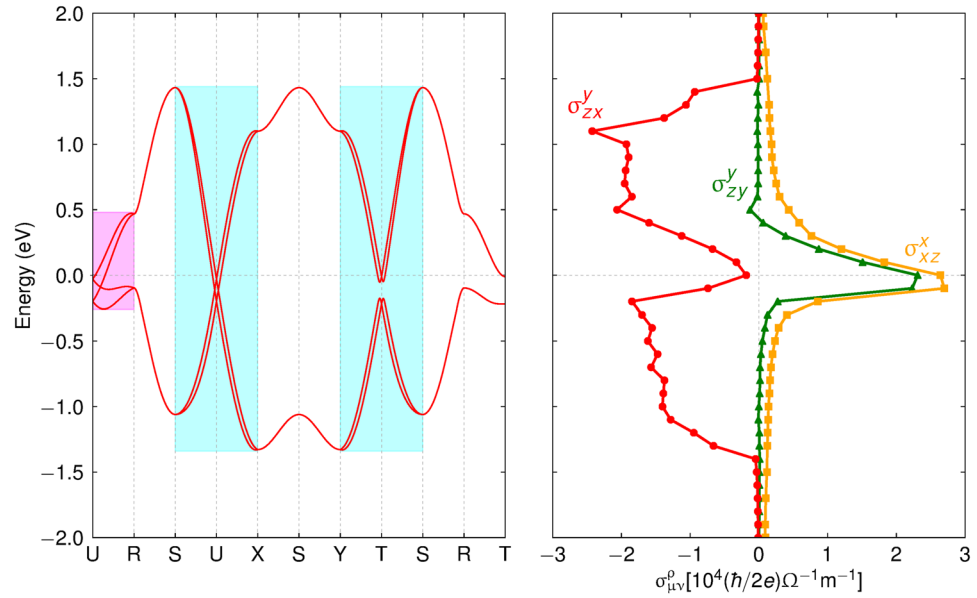


**Figure 2.** Electron energy band structure (left) and spin Hall conductivity (right) in the bulk system. The magenta and cyan boxes highlight the nearly degenerate bands that extend from the nodal ring structure. Spin Hall conductivity  $\sigma_{\mu\nu}^{\rho}$  is presented as a function of the Fermi level  $\epsilon_F$  (vertical axis) for three configurations in which the system shows the largest response:  $\sigma_{zx}^y$  (red dot),  $\sigma_{zy}^y$  (green triangle),  $\sigma_{xz}^x$  (orange square). Here,  $x, y, z$  represent the pseudo-cubic axes of the system.

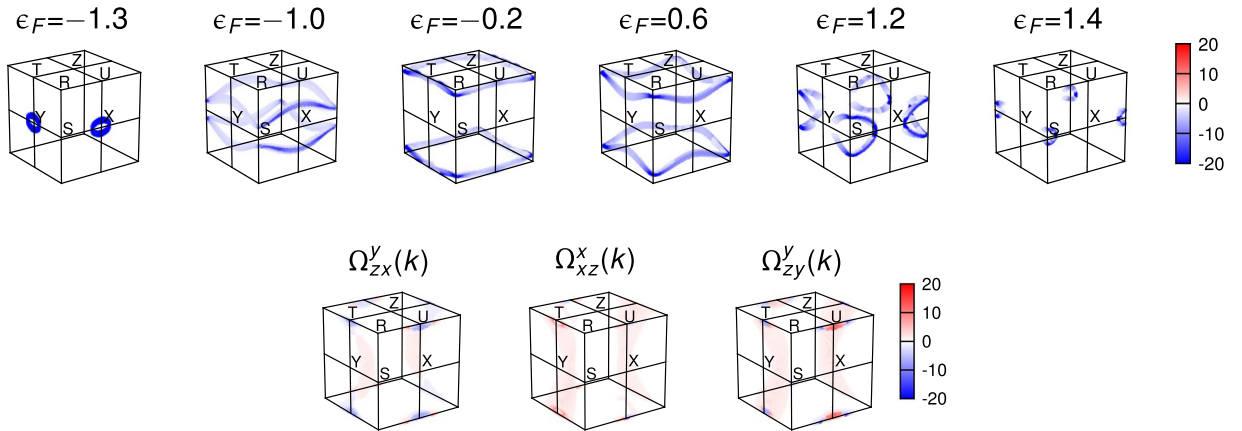


**Figure 3.** Momentum-resolved bulk spin Hall conductivity. Top:  $\Omega_{zx}^y(\mathbf{k})$  as a function of the Fermi level  $\epsilon_F$ . Bottom:  $\Omega_{\mu\nu}^{\rho}(\mathbf{k})$  at  $\epsilon_F = 0$  for the three configurations shown in Fig. 2.

**Electronic Origin of Large Bulk SHC.** Momentum-resolved spin Hall conductivity provides further useful information about the origin of the large spin Hall effect. Defining momentum-resolved spin Hall conductivity  $\Omega_{\mu\nu}^{\rho}(\mathbf{k})$  by  $\sigma_{\mu\nu}^{\rho} = \sum_{\mathbf{k}} \Omega_{\mu\nu}^{\rho}(\mathbf{k})$ , we investigate the distribution of  $\Omega_{\mu\nu}^{\rho}(\mathbf{k})$  in the Brillouin zone. First, we find that high intensity of  $\Omega_{zx}^y(\mathbf{k})$  appears in the form of loops extended over the  $k_a = \pi$  and  $k_b = \pi$  planes as shown in Fig. 3 (top). The  $\mathbf{k}$ -points of the loops have the same sign of  $\Omega_{zx}^y(\mathbf{k})$ , thus leading to constructive contributions to  $\sigma_{zx}^y$ . Remarkably, these loops correspond to the  $\mathbf{k}$ -points where the Fermi level crosses the nearly degenerate bands in the  $k_a = \pi$  and  $k_b = \pi$  planes [compare the resemblance of the Fermi surface cross sections within the  $k_b = \pi$  plane in Fig. 1 to  $\Omega_{zx}^y(\mathbf{k})$  in Fig. 3 (top)]. This suggests that the ‘active’ electronic states that are contributing the most to  $\Omega_{zx}^y(\mathbf{k})$  are in fact the states residing in the nearly degenerate band structure in the  $k_a = \pi$  and  $k_b = \pi$  planes. Therefore, one can conclude that the large values of  $\sigma_{zx}^y$  indeed originates from the interband transition between the aforementioned nearly degenerate bands in the  $k_a = \pi$  and  $k_b = \pi$  planes (shaded in Fig. 2).

The different behaviours of  $\sigma_{zx}^y, \sigma_{zy}^y, \sigma_{xz}^x$  around the zero Fermi energy (Fig. 2) can also be understood by investigating the corresponding  $\Omega_{\mu\nu}^{\rho}(\mathbf{k})$ . As shown in Fig. 3 (bottom), spin Hall conductivity at  $\epsilon_F = 0$  eV has major contributions broadly from two different parts of the Brillouin zone: (i) a region around the U point and (ii) arch-shaped interior regions connected to the T point. Specifically, in the case of  $\Omega_{zx}^y(\mathbf{k})$ , the two parts have a

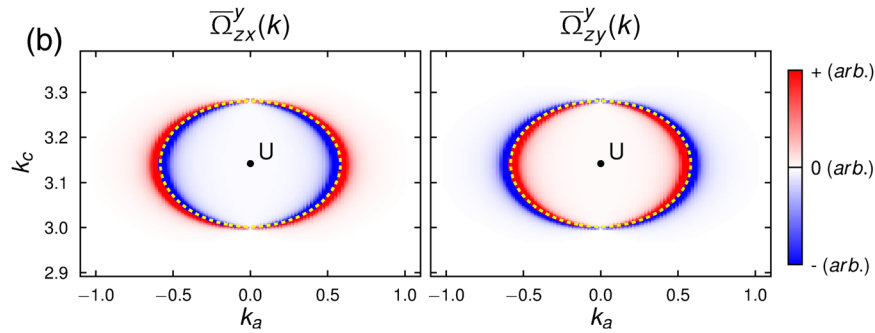


**Figure 4.** Spin-Berry curvature of the nodal ring band structure. The color maps depict the net spin-Berry curvature  $\bar{\Omega}_{\mu\nu}^y(\mathbf{k})$  ( $=\sum_{n=1}^4[\Omega_{\mu\nu}^y]_{nk}$ ) calculated for the lowest two doubly degenerate bands on the  $k_b = \pi$  plane [Figs. 1(c) and 2]. The yellow dashed line denotes the nodal ring residing in the  $k_b = \pi$  plane.

different sign and their contributions to spin Hall conductivity almost cancel each other, which results in highly suppressed  $\sigma_{zx}^y$  at  $\varepsilon_F = 0$  eV. However, the other two cases  $\Omega_{zy}^y(\mathbf{k})$  and  $\Omega_{xz}^x(\mathbf{k})$  have an almost uniform sign over the two parts, thereby  $\sigma_{zy}^y$  and  $\sigma_{xz}^x$  have a large value at  $\varepsilon_F = 0$  eV.

**Spin-Berry Curvature around Nodal Ring.** Now we examine the spin-Berry curvature contained in the nodal ring band structure and its contribution to the bulk SHC. Figure 4 depicts the spin-Berry curvature of the nodal ring band structure. High intensity spin-Berry curvature is found near the nodal ring band crossing. Moreover, the sign of the spin-Berry curvature changes across the nodal ring in the  $k_b = \pi$  plane (such sign-changing behaviour of high intensity spin-Berry curvature across band crossing points has also been found in recent *ab initio* studies on Weyl semimetals<sup>39</sup>). One interesting feature here is that the spin-Berry curvature is nonzero only at the  $k_b = \pi$  plane, and it immediately vanishes off the plane.

Although the nodal ring structure generates high intensity of spin-Berry curvature (near the ring), its net contribution to the total bulk SHC is quite small due to the massive cancellation between the opposite signs of the spin-Berry curvature in the  $k_b = \pi$  plane. We directly examine this large cancellation by focusing on the nodal ring's isolated contributions (i.e., from the  $\mathbf{k}$ -points in the rectangular region just-enclosing the nodal ring in the  $k_b = \pi$  plane). For the three configurations,  $\sigma_{zx}^y$ ,  $\sigma_{zy}^y$  and  $\sigma_{xz}^x$ , the isolated contribution (weighted by the entire Brillouin zone contribution) of the nodal ring is 6%, 0.7%, and 0.03% respectively for  $\varepsilon_F = 0$  eV, and 7%, 2%, and 0.01% respectively for  $\varepsilon_F = -0.1$  eV. Furthermore, we also investigated the impact of the size of the nodal ring (controlled by the spin-dependent hopping parameter  $t_d^y$ ) on the SHC. Our computations determined that despite the size of the nodal ring increasing by two-fold, four-fold or even six-fold, the change in the SHC is very small and not substantial (order of magnitude remains the same). This suggests that any contributions arising from and about the the nodal ring are promptly cancelled, resulting in its benign contribution to the SHC.

### Impact of Breaking Nonsymmorphic Symmetries on Bulk SHC

In a realistic system, it is highly probable (and likely) that one or many of nonsymmorphic symmetries can be broken. The breaking of these symmetries (such as the glide symmetries) can be the result of growth defects, impurities, or external strain/pressure on the bulk. This can lead to, depending on which symmetry is broken, the lifting of degeneracy at certain high symmetry locations in the Brillouin zone or (even more drastically) the removal of certain topological features in the band structure like the nodal ring. In fact, the gapping of the nodal ring is not a rare occurrence in thin film configurations of SrIrO<sub>3</sub> as has been observed through angle-resolved photoemission spectroscopy (ARPES) studies on epitaxial thin films<sup>40</sup>, as well as in epitaxially strained thin films<sup>38</sup>. One way to incorporate such a broken symmetry is a perturbation term in the bulk model:

$$h_{gap} = t_{gap}[\sin(k_y) - \sin(k_x)]\sin(k_z)\nu_y\tau_y. \quad (4)$$

This term preserves the inversion, time-reversal, and mirror symmetries. However, it breaks the  $b$ -glide and  $n$ -glide symmetries, and so it meets the required criterion to completely gap out the nodal ring. This can be seen by the commutation of  $h_{gap}$  and the symmetry operators (Eq. S3 in Supplementary B). Moreover, this term involves the in-plane and sublayer degrees of freedom ( $\tau$  and  $\nu$ , respectively) and so physically this mimics a possible physical strain on the system that has led to the breaking of these symmetries. The choice of  $t_{gap} = 0.01$  eV is at least an order of magnitude smaller than the other energy scales in the system, and thus it acts as a small perturbation. Furthermore, this term introduces a Dirac mass gap of  $\approx 40$  meV, consistent with experimental observations of gapped Dirac points in SrIrO<sub>3</sub> thin films<sup>40</sup>. Figure S4 in Supplementary E depicts the impact of the perturbative term  $h_{gap}$  on the band structure (along high symmetry directions  $U \rightarrow R$  and  $U \rightarrow X$ ).

However,  $h_{gap}$  is only one of a myriad of possible symmetry breaking terms that could be introduced, involving again only the in-plane and sublayer degrees of freedom. We limit our possibilities to terms that can modify the band structure in regions of the Brillouin zone that contribute the most to the spin Hall conductivity (highlighted in Fig. 2); these are the terms that have the greatest chance in modifying the spin Hall conductivities. In particular, we determined two types of symmetry breaking terms that introduced qualitative changes in the band structure, and thus potentially had the chance to introduce a non-zero change in the spin Hall conductivities:

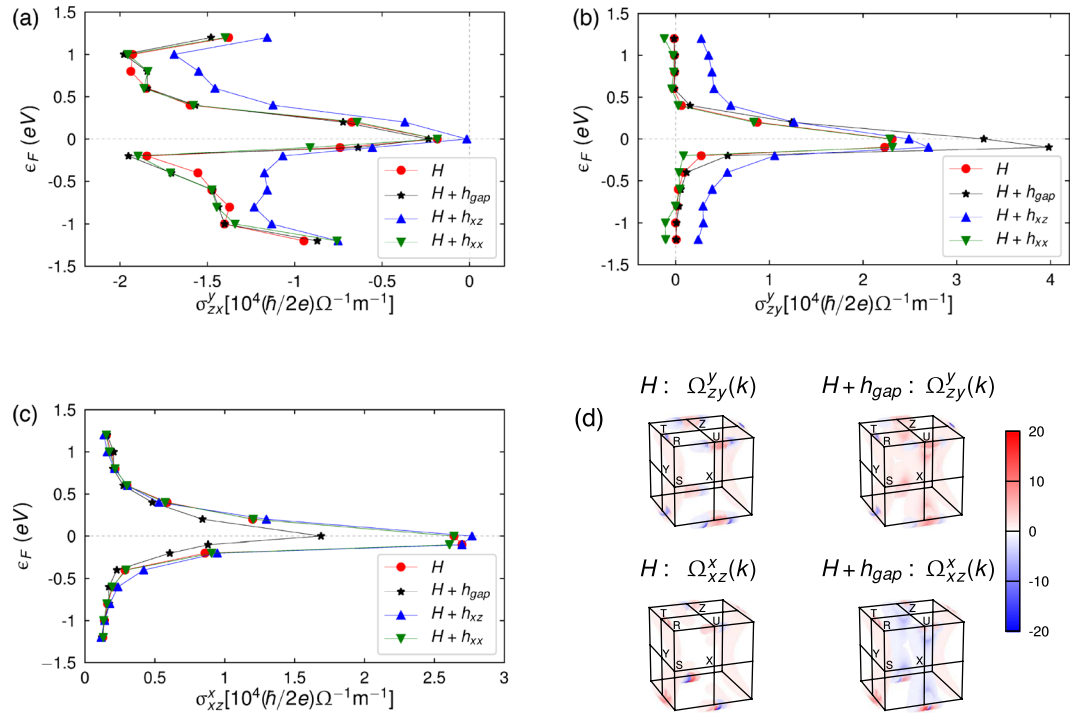


**Figure 5.** Bulk spin Hall conductivity in the presence of symmetry-breaking perturbations. **(a,b,c)**  $\sigma_{zx}^y$ ,  $\sigma_{zy}^y$ ,  $\sigma_{xz}^x$  as functions of the Fermi level  $\epsilon_F$  for the three symmetry-broken bulk systems ( $H + h_{gap}$ ,  $H + h_{xz}$ ,  $H + h_{xx}$ ). **(d)**  $\Omega_{zy}^y(k)$  and  $\Omega_{xz}^x(k)$  of the system  $H + h_{gap}$  for the zero Fermi level.

$$\begin{aligned} h_{xx} &= t_{xx}[\sin(k_y) - \sin(k_x)]\sin(k_z)\nu_x\tau_x, \\ h_{xz} &= t_{xz}[\sin(k_y) + \sin(k_x)]\sin(k_z)\nu_x\tau_z. \end{aligned} \quad (5)$$

These terms break  $n$ -glide and  $m$  symmetries, while preserving  $b$ -glide symmetry. The choice of  $t_{xx,xz} = 0.05 eV$  was taken as it ensured that these terms act as perturbations on the original bulk model, while also creating a qualitative change in the band structure (Figs. S5, S6 in Supplementary E). Augmenting the original Hamiltonian with these perturbative terms, we present the spin Hall conductivities of the three configurations for which the system had the greatest response in Fig. 5(a)–(c).

Interestingly, despite the inclusion of various symmetry breaking perturbative terms, the component  $\sigma_{zx}^y$  remains stable and still maintains the large spin Hall conductivity at all the previously noted Fermi levels. This is not altogether surprising as the greatest contributions to this component arise from the nearly degenerate electron band structure (cyan in Fig. 2). Since the perturbative terms  $h_{gap}$  and  $h_{xx}$  do not affect the nearly degenerate regions, the spin Hall conductivity magnitude is preserved with the inclusion of these terms. However, there is a small modification, but remains within the same order of magnitude, in the spin Hall conductivity due to  $h_{xz}$ . This term marginally changes the band structure in the nearly degenerate regions by only lifting the degeneracy at the band crossing T point. On the other hand, the components  $\sigma_{zy}^y$  and  $\sigma_{xz}^x$  do see a jump in the spin Hall conductivity by the gapping of the nodal ring close to the zero energy level; apart from  $\sigma_{zy}^y$  experiencing a similar shift as  $\sigma_{zx}^y$  due to  $h_{xz}$ , these configurations are stable to the other perturbations. By considering the momentum-resolved SHC at the zero energy level [Fig. 5(d)] one notices new arch-like features that develop about the U point. For  $\sigma_{zy}^y$ , the new features have the same sign as the arch-like features from the non-perturbed model and so the spin Hall conductivity is enlarged; while for  $\sigma_{xz}^x$ , the new features have the opposite sign and so diminish the spin Hall conductivity. Nevertheless, the enlargement/diminishment is not substantial and the spin Hall conductivity remains within the same order of magnitude. Hence, the bulk spin Hall conductivity is stable and robust to the introduction of various symmetry breaking terms (other symmetry breaking terms further support this conclusion).

### Spin Hall Effect in Thin Film System

Now we turn our attention to thin film systems of SrIrO<sub>3</sub>. Recent experiments<sup>32</sup> discovered that SrIrO<sub>3</sub> thin films exhibit surprisingly large spin Hall conductivity [ $\sigma_{SH}^{exp} \sim 10^5 (\hbar/2e) \Omega^{-1} \text{m}^{-1}$ ], which is about one order of magnitude larger than values predicted for the bulk system. The experimental film samples were grown along the [010]<sub>c</sub> direction up to a thickness of 20 bulk unit cells. Due to the nature of the experimental setup, only the spin current induced along the [010]<sub>c</sub> film direction was measured (see Fig. 6). This large thin film spin Hall response is unexpected, since our theory for the bulk system predicts rather small responses for the same configuration corresponding to the experiment.

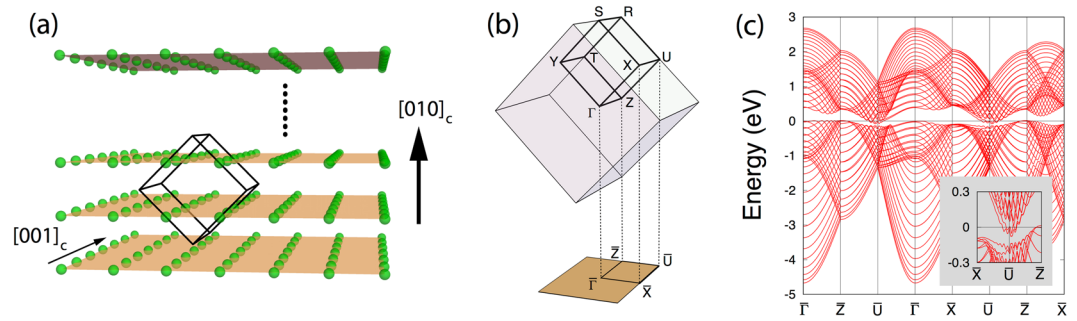


**Figure 6.** Geometry and electronic structure of  $(010)_c$  thin film. (a) Lattice geometry of Ir ions (green). The orange planes describe a stacking of  $(010)_c$  layers of Ir ions in thin film system. The black lines and arrows represent bulk unit cell and some of the crystallographic axes, respectively. (b) Two dimensional Brillouin zone of  $(010)_c$  film. The bulk Brillouin zone (cube) is projected and folded into the film Brillouin zone (bottom rectangle). (c) Electronic energy band structure of  $(010)_c$  film with 16 layers of Ir ions. The inset shows the band structure magnified around the  $\bar{U}$  point.

In this section, we study the  $(010)_c$  thin film system to get an insight into the large enhancement of SHC in the film geometry. The  $(010)_c$  thin film in our study is described using the bulk tight-binding model  $H$  on the slab lattice geometry shown in Fig. 6(a). Our calculation results presented below were obtained for the system with 16 layers of Ir sites (8 bulk unit cells along the  $[010]_c$  direction) which is the largest thickness that allowed us to reach convergence in the SHC calculations within a reasonable amount of time. The finite thickness of the film system leads to the breaking of some of the original bulk symmetries, for instance the  $n$ -glide and  $b$ -glide symmetries as well as the translational symmetry along the  $[010]_c$  direction (see Table 1 for the remaining symmetries in the film system). As a consequence of the lower lattice symmetry, the nodal line band crossing of the bulk system is gapped out in the  $(010)_c$  film [see Fig. 6(c)]. Moreover, the film system has a nonuniform electron distribution over the layers of the Ir sites as shown in Fig. S7 in Supplementary F (by contrast, the bulk system has a uniform electron distribution over the four sublattices by lattice symmetry).

Figure 7(a) displays the spin Hall conductivity obtained from the linear response theory for the thin film. Our result shows large film SHC in the configuration corresponding to the experiments:  $\sigma_{yx}^z \sim 10^4 (\hbar/2e) \Omega^{-1} m^{-1}$  around the zero Fermi energy [see the shaded region in Fig. 7(a)]. However, in the same configuration, the bulk system shows rather small SHC as shown in the figure (at least one order of magnitude smaller compared to the film SHC). Thus, natural questions to ask are (i) why is the film's spin Hall response so different from the bulk system and (ii) what is the origin of the large spin Hall response in the film.

To understand the difference between the film and bulk and the origin of the large SHC in the film, we resolve the SHC in the two dimensional Brillouin zone of the film as shown in Fig. 7(b). The upper and lower panels represent the momentum-resolved SHC  $\Omega_{yx}^z(\mathbf{k})$  for the film and bulk systems, respectively; the bulk result was obtained by taking into account the zone folding described in Fig. 6(b). The similarities and differences between the film and bulk systems are revealed in the distribution of  $\Omega_{yx}^z(\mathbf{k})$ . Firstly at each Fermi energy, overall patterns of  $\Omega_{yx}^z(\mathbf{k})$  in the film and bulk are quite similar to each other. Despite this similarity, significant difference in the magnitude and sign of  $\Omega_{yx}^z(\mathbf{k})$  is observed between the film and bulk, suggesting that electron wave functions in the thin film significantly deviate from wave functions in the corresponding bulk system.

In addition to the modification of electron wave functions, the surface states arising in the film (which are localized around the boundary surfaces) could be another source for the difference between the film and bulk spin Hall responses. Figure 7(c) depicts the locations at which surface states occur in the Brillouin zone. Comparing Figs. 7(b,c), one observes that the distribution of the surface states in momentum space does not seem to match well with the pattern of  $\Omega_{yx}^z(\mathbf{k})$  in the film system. This supports the idea that the large film SHC is mainly an effect of bulk-like electron states rather than the surface states. The bulk-like electron states are, however, substantially modified from states in the bulk system as indicated by the electron density (Fig. S7 in Supplementary F) and spin-Berry curvature distribution [Fig. 7(b)]. The change in the wave functions (and subsequent enhancement of the spin Hall effect in the film geometry) is attributed to the lower lattice symmetry in the thin film system. In the absence of the film direction translation,  $n$ -glide,  $b$ -glide, and other lattice symmetries, electron wave functions are obviously less constrained as compared to in the original bulk environment.

## Conclusions

In this work, we examined the intrinsic spin Hall effect in both bulk and thin film configurations of SrIrO<sub>3</sub> using linear response theory. We employed the  $j_{\text{eff}} = 1/2$  tight binding model constructed from *ab initio* studies of SrIrO<sub>3</sub><sup>28,29</sup>. From our bulk SrIrO<sub>3</sub> studies, we found an unexpectedly large spin Hall conductivity [ $\sigma_{\text{SH}} \sim 10^4 (\hbar/e) (\Omega m)^{-1}$ ] in three configurations:  $\sigma_{zx}^y$ ,  $\sigma_{zy}^x$ , and  $\sigma_{xz}^x$ . We attribute the enormity of this response to large extended regions in the Brillouin zone (shaded in Fig. 2) where the band structure is nearly degenerate. We also determined that the bulk spin Hall conductivity is very robust and stable to a number of symmetry breaking terms, provided that the aforementioned nearly degenerate band structure is preserved. Our thin film calculations implicated the modification of the bulk-like wave functions in the thin film to be responsible for enhanced SHE in certain geometries. This thin film consideration is unlike the symmetry-broken-augmented bulk calculations where the symmetry breaking perturbations do not induce

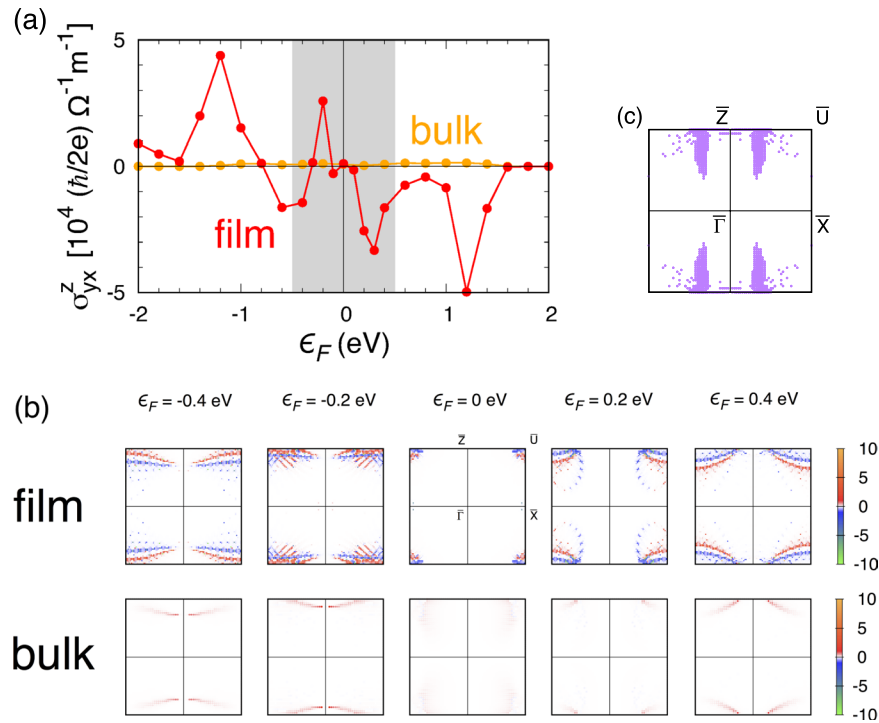


**Figure 7.** (a) Spin Hall conductivity  $\sigma_{yx}^z$  of the thin film as a function of Fermi energy  $\epsilon_F$ . Corresponding bulk SHC is shown for comparison. (b) Momentum-resolved spin Hall conductivity  $\Omega_{yx}^z(\mathbf{k})$  of the thin film (upper) and bulk (lower) systems. The bulk result was obtained by taking into account the zone folding described in Fig. 6(b) and using the same unit for the film and bulk results for comparison with the film result. (c) Locations of the surface states in the Brillouin zone. The purple dots represent the states with electron density with more than 66 percent at the top four and bottom four layers among the entire 16 Ir-layers of the film system. The surface state locations, which are qualitatively different from the pattern of  $\Omega_{yx}^z(\mathbf{k})$  in Fig. 7(b), indicate that the large film SHE is mainly an effect by bulk-like states rather than the surface states in the thin film system.

as large a change to the electronic states. The nature of the electronic states being a key ingredient in the spin Hall conductivity suggests that further constrained and restricted geometries of SrIrO<sub>3</sub> (where the electronic states can change significantly due to, for example, certain symmetries being decisively broken) can lead to large enhancement of the spin Hall conductivity with respect to the corresponding bulk response. Although this study examines the case of SrIrO<sub>3</sub>, we are hopeful that similar 5d-like iridate materials can also have large spin Hall conductivities. This aspiration is partly rooted in recent experimental work in binary 5d transition metal oxide IrO<sub>2</sub>, where large SHE was demonstrated with high spin current conversion<sup>24</sup>.

The results from our theoretical calculations seem to agree at least qualitatively with the recent experimental report where large spin Hall conductivity was observed in SrIrO<sub>3</sub> thin films. To enable a more quantitative comparison with experimental spin Hall conductivity measurements, it is important to take into account the effects of the neighbouring ferromagnetic permalloy layer (Py) on the SHC. Although we provide some early analysis of these effects in Supplementary G, we propose taking into account the effects of the Py exchange field on the interface to be an interesting direction for future research.

## Methods

The SHC is computed by numerically integrating Eq. 2 on a uniform  $k$ -mesh over the Brillouin zone. To ensure satisfactory convergence, we chose fine  $k$ -grid meshes of (at least)  $140 \times 140 \times 140$  for the bulk calculations, and  $100 \times 100$  for the thin film systems.

## References

1. Sinova, J., Valenzuela, S. O., Wunderlich, J., Back, C. H. & Jungwirth, T. Spin Hall effects. *Rev. Mod. Phys.* **87**, 1213–1260 (2015).
2. Nagaosa, N., Sinova, J., Onoda, S., MacDonald, A. H. & Ong, N. P. Anomalous Hall effect. *Rev. Mod. Phys.* **82**, 1539–1592 (2010).
3. Hirsch, J. E. Spin Hall Effect. *Phys. Rev. Lett.* **83**, 1834–1837 (1999).
4. Sinova, J. *et al.* Universal Intrinsic Spin Hall Effect. *Phys. Rev. Lett.* **92**, 126603 (2004).
5. Žutić, I., Fabian, J. & Das Sarma, S. Spintronics: Fundamentals and applications. *Rev. Mod. Phys.* **76**, 323–410 (2004).
6. Jungwirth, T., Wunderlich, J. & Olejník, K. Spin Hall effect devices. *Nature Materials* **11**, 382–390 (2012).
7. Murakami, S., Nagaosa, N. & Zhang, S.-C. Dissipationless Quantum Spin Current at Room Temperature. *Science* **301**, 1348–1351 (2003).
8. Liu, L., Buhrman, R. A. & Ralph, D. C. Review and Analysis of Measurements of the Spin Hall Effect in Platinum. ArXiv e-prints (2011).
9. Tanaka, T. *et al.* Intrinsic spin hall effect and orbital Hall effect in 4d and 5d transition metals. *Phys. Rev. B* **77**, 165117 (2008).
10. Kontani, H., Tanaka, T., Hirashima, D. S., Yamada, K. & Inoue, J. Giant Orbital Hall Effect in Transition Metals: Origin of Large Spin and Anomalous Hall Effects. *Phys. Rev. Lett.* **102**, 016601 (2009).



11. Kimura, T., Otani, Y., Sato, T., Takahashi, S. & Maekawa, S. Room-Temperature Reversible Spin Hall Effect. *Phys. Rev. Lett.* **98**, 156601 (2007).
12. Guo, G. Y., Murakami, S., Chen, T.-W. & Nagaosa, N. Intrinsic Spin Hall Effect in Platinum: First-Principles Calculations. *Phys. Rev. Lett.* **100**, 096401 (2008).
13. Morota, M. *et al.* Indication of intrinsic spin Hall effect in 4d and 5d transition metals. *Phys. Rev. B* **83**, 174405 (2011).
14. Liu, L., Moriyama, T., Ralph, D. C. & Buhrman, R. A. Spin-Torque Ferromagnetic Resonance Induced by the Spin Hall Effect. *Phys. Rev. Lett.* **106**, 036601 (2011).
15. Liu, L., Lee, O. J., Gudmundsen, T. J., Ralph, D. C. & Buhrman, R. A. Current-Induced Switching of Perpendicularly Magnetized Magnetic Layers Using Spin Torque from the Spin Hall Effect. *Phys. Rev. Lett.* **109**, 096602 (2012).
16. Yao, Y. & Fang, Z. Sign Changes of Intrinsic Spin Hall Effect in Semiconductors and Simple Metals: First-Principles Calculations. *Phys. Rev. Lett.* **95**, 156601 (2005).
17. Seki, T. *et al.* Giant spin Hall effect in perpendicularly spin-polarized FePt/Au devices. *Nature Materials* **7**, 125–129 (2008).
18. Guo, G.-Y., Maekawa, S. & Nagaosa, N. Enhanced Spin Hall Effect by Resonant Skew Scattering in the Orbital-Dependent Kondo Effect. *Phys. Rev. Lett.* **102**, 036401 (2009).
19. Seki, T., Sugai, I., Hasegawa, Y., Mitani, S. & Takahashi, K. Spin Hall effect and Nernst effect in FePt/Au multi-terminal devices with different Au thicknesses. *Solid State Communications* **150**, 496–499 (2010).
20. Niimi, Y. *et al.* Extrinsic spin hall effects measured with lateral spin valve structures. *Phys. Rev. B* **89**, 054401 (2014).
21. Ando, K. & Saitoh, E. Inverse spin-hall effect in palladium at room temperature. *Journal of Applied Physics* **108**, 113925 (2010).
22. Mellnik, A. R. *et al.* Spin-transfer torque generated by a topological insulator. *Nature* **511**, 449–451 (2014).
23. Fan, Y. *et al.* Magnetization switching through giant spin-orbit torque in a magnetically doped topological insulator heterostructure. *Nature Materials* **13**, 699–704 (2014).
24. Fujiwara, K. *et al.* 5d iridium oxide as a material for spin-current detection. *Nature Communications* **4**, 2893 (2013).
25. Wan, X., Turner, A. M., Vishwanath, A. & Savrasov, S. Y. Topological semimetal and Fermi-arc surface states in the electronic structure of pyrochlore iridates. *Phys. Rev. B* **83**, 205101 (2011).
26. Ueda, K. *et al.* Magnetic field-induced insulator-semimetal transition in a pyrochlore Nd<sub>2</sub>Ir<sub>2</sub>O<sub>7</sub>. *Phys. Rev. Lett.* **115**, 056402 (2015).
27. Tian, Z. *et al.* Field-induced quantum metal-insulator transition in the pyrochlore iridate Nd<sub>2</sub>Ir<sub>2</sub>O<sub>7</sub>. *Nature Physics* **12**, 134–138 (2016).
28. Carter, J.-M., Shankar, V. V., Zeb, M. A. & Kee, H.-Y. Semimetal and Topological Insulator in Perovskite Iridates. *Phys. Rev. B* **85**, 115105 (2012).
29. Chen, Y., Lu, Y.-M. & Kee, H.-Y. Topological crystalline metal in orthorhombic perovskite iridates. *Nature Communications* **6**, 6593 (2015).
30. Sushkov, A. B. *et al.* Optical evidence for a Weyl semimetal state in pyrochlore Eu<sub>2</sub>Ir<sub>2</sub>O<sub>7</sub>. *Phys. Rev. B* **92**, 241108 (2015).
31. Ueda, K. *et al.* Variation of Charge Dynamics in the Course of Metal-Insulator Transition for Pyrochlore-Type Nd<sub>2</sub>Ir<sub>2</sub>O<sub>7</sub>. *Phys. Rev. Lett.* **109**, 136402 (2012).
32. Nan, T. *et al.* (unpublished) (2017).
33. Chen, Y., Kim, H.-S. & Kee, H.-Y. Topological crystalline semimetals in nonsymmorphic lattices. *Phys. Rev. B* **93**, 155140 (2016).
34. Fang, C., Chen, Y., Kee, H.-Y. & Fu, L. Topological nodal line semimetals with and without spin-orbital coupling. *Phys. Rev. B* **92**, 081201 (2015).
35. Rhim, J.-W. & Kim, Y. B. Landau level quantization and almost flat modes in three-dimensional semimetals with nodal ring spectra. *Phys. Rev. B* **92**, 045126 (2015).
36. Rhim, J.-W. & Kim, Y. B. Anisotropic density fluctuations, plasmons, and Friedel oscillations in nodal line semimetal. *New Journal of Physics* **18**, 043010 (2016).
37. Huh, Y., Moon, E.-G. & Kim, Y. B. Long-range Coulomb interaction in nodal-ring semimetals. *Phys. Rev. B* **93**, 035138 (2016).
38. Liu, J. *et al.* Strain-induced nonsymmorphic symmetry breaking and removal of dirac semimetallic nodal line in an orthoperovskite iridate. *Phys. Rev. B* **93**, 085118 (2016).
39. Sun, Y., Zhang, Y., Felser, C. & Yan, B. Strong intrinsic spin Hall effect in the TaAs family of Weyl semimetals. *Phys. Rev. Lett.* **117**, 146403 (2016).
40. Liu, Z. T. *et al.* Direct observation of the Dirac nodes lifting in semimetallic perovskite SrIrO<sub>3</sub> thin films. *Scientific Reports* **6**, 30309 (2016).
41. Loken, C. *et al.* Scinet: Lessons Learned from Building a Power-efficient Top-20 System and Data Centre. *Journal of Physics: Conference Series* **256**, 012026 (2010).

## Acknowledgements

K. H. and Y. B. K. thank T. Nan, T. J. Anderson, C. B. Eom, M. S. Rzchowski, J. Gibbons, and D. C. Ralph for helpful discussions and collaborations in a related study. We would like to thank Yige Chen and Choong Hyun Kim for useful discussions. This work was supported by the NSERC of Canada and the Center for Quantum Materials at the University of Toronto. We acknowledge the hospitality at the Kavli Institute for Theoretical Physics, supported in part by the NSF grant PHY-1125915 and the Aspen Center for Physics, supported in part by NSF grant PHY-1607611, where some parts of this work were done. H.W.L. was supported by the National Research Foundation of Korea (NRF) grant (No. 2011-0030046). Some of the computations were performed on the GPC supercomputer at the SciNet HPC Consortium<sup>41</sup>. SciNet is funded by: the Canada Foundation for Innovation under the auspices of Compute Canada; the Government of Ontario; Ontario Research Fund - Research Excellence; and the University of Toronto.

## Author Contributions

Y.B.K. and H.-W.L. conceived the study, and A.S.P. and K.H. performed calculations under supervision of Y.B.K. and H.-W.L. All authors participated in writing the manuscript.

## Additional Information

**Supplementary information** accompanies this paper at <https://doi.org/10.1038/s41598-018-26355-y>.

**Competing Interests:** The authors declare no competing interests.

**Publisher's note:** Springer Nature remains neutral with regard to jurisdictional claims in published maps and institutional affiliations.



**Open Access** This article is licensed under a Creative Commons Attribution 4.0 International License, which permits use, sharing, adaptation, distribution and reproduction in any medium or format, as long as you give appropriate credit to the original author(s) and the source, provide a link to the Creative Commons license, and indicate if changes were made. The images or other third party material in this article are included in the article's Creative Commons license, unless indicated otherwise in a credit line to the material. If material is not included in the article's Creative Commons license and your intended use is not permitted by statutory regulation or exceeds the permitted use, you will need to obtain permission directly from the copyright holder. To view a copy of this license, visit <http://creativecommons.org/licenses/by/4.0/>.

© The Author(s) 2018